A dynamic phase field model with no attenuation of wave speed for rapid fracture instability in hyperelastic materials

Fucheng Tian [a,b], Jun Zeng [a,b], Xiaoliang Tang [a,b], Tingyu Xu [a,b], Liangbin Li [a,b,c,]*

[a] National Synchrotron Radiation Lab, University of Science and Technology of China, Hefei 230029, China
[b] Anhui Provincial Engineering Laboratory of Advanced Functional Polymer Film, University of Science and Technology of China, Hefei 230029, China
[c] CAS Key Laboratory of Soft Matter Chemistry, University of Science and Technology of China, Hefei 230029, China

ABSTRACT

Numerical experiments on phase field modeling of the fracture in pre-strained hyperelastic materials reveal that the classical mechanical-based dynamic phase field model is ineffective in the framework of non-linear deformation. The aspiration to gain insight into rapid fracture instability motivated us to develop a novel dynamic phase field model characterized by wave velocity invariance, enabling crack propagation at a velocity approach to the asymptotic limit. Given that the numerical treatment of rapid fractures involves extremely high spatiotemporal resolution, robust explicit dynamics and a tried-and-tested multi-level hybrid adaptive mesh algorithm are invoked. More crucially, an original adaptive distorted mesh removal scheme (ADMR) was developed to cope with the intractable finite element mesh distortion problem in large deformation fractures. The detailed numerical implementation for entire procedures is outlined, and its reliability is verified by two quasi-static fracture benchmarks. Utilizing the proposed model and innovative algorithms, the arresting ultrahigh-speed crack oscillation and tip-splitting instabilities captured in the fracture experiments of brittle gels were successfully reproduced. The critical crack velocity at the onset of the instability is also identified, close to the experimental measurements.

© 2020 Elsevier Ltd. All rights reserved.

1. Introduction

Fast-moving cracks in hyperelastic materials like gels have stimulated intense research interest for decades due to their multiplicate dynamic nature (Bouchbinder et al., 2005; Fineberg and Marder, 1999; Livne et al., 2008; Livne et al., 2010; Livne et al., 2005). At the crack velocity reaches a critical velocity of $V_{mb} \sim 0.4\, V_R$ (Rayleigh wave velocity, V_R), a straight crack first undergoes micro-branching instability in three dimensions, characterized by the emergence of the frustrated crack branching on the fracture surface (Fineberg et al., 1997; Fineberg et al., 1991; Ravi-Chandar and Knauss, 1984; Sharon et al., 1995). Beyond the threshold V_{mb}, dynamic cracks enter into a bistable region where single or multiple cracks can persist (Bouchbinder et al., 2014). After suppressing the onset of micro-branching instability by thinning the specimen, a single crack can be accelerated to approach its theoretical limit in very large background strains. However, a new and intriguing crack oscillation instability with two-dimension (2D) nature emerges at a much higher critical velocity of $V_{osc} \sim 0.9\, V_S$ (shear wave velocity, V_S)

(Bouchbinder, 2009b; Goldman et al., 2012; Livne et al., 2007). If the background strain is further heightened, an ultra-high-speed tip-splitting instability that is in sharp contrast with the previous low-speed bifurcation will arise either in the wake of or prior to the oscillatory crack states (Lubomirsky et al., 2018). Because of such rich dynamics, figuring out the underlying laws is of twofold significance in fundamental and applied research.

Considerable progress to date has been obtained in the study of simple crack motions, the well-established of which is the classical linear elastic fracture mechanics (LEFM) (Broberg, 1999; Freund, 1998; Ravi-Chandar, 2004). LEFM is grounded in several fundamental assumptions, which is essentially a scale-free theory. A small-scale region with complicated dissipation or nonlinear deformation at the crack tip ('progress zone') is not account for in the framework of this theory (Bouchbinder et al., 2010a). However, recent experiments manifested that this supplementary scale is of prominent effect on crack dynamics, especially for the unstable cracks (Bouchbinder et al., 2014; Buehler et al., 2003; Buehler and Gao, 2006). As a result of that, once a simple crack state loses stability, e.g. micro-branching or oscillation, LEFM is no longer valid (Chen et al., 2017). A self-contained theoretical framework for dynamic cracks should certainly contain at least this inherent scale. An authenticated weakly non-linear theory that absorbed a

* Corresponding author at: National Synchrotron Radiation Lab, University of Science and Technology of China, Hefei 230029, China.
    E-mail address: lbli@ustc.edu.cn (L. Li).

non-linear length scale l_{nl} was born for this end (Bouchbinder et al., 2008, 2010b). Nevertheless, this theory alone falls short of predicting the crack path. We learned that a class of phase field models (PFM) within the category of the diffusive crack models were developed over the last decade (Bourdin et al., 2008; Francfort and Marigo, 1998; Henry and Levine, 2004; Karma et al., 2001). By virtue of the advantage of not requiring to track sharp cracked surfaces, PFM shows a promising prospect for dealing with the complex cracks, such as crack branching (Bleyer and Molinari, 2017; Karma and Lobkovsky, 2004).

Several phase field models with different theoretical origins have been developed in the physics and mechanics communities, respectively. The phase field idea in the physical community roots in the Ginzburg-Landau phase transition theory (Aranson et al., 2000; Hakim and Karma, 2009; Karma et al., 2001), which has been demonstrated to be fruitful in predicting crack morphology and path selection. In contrast, the idea in the mechanics community is to construct a variational approach to brittle fracture based on classic Griffith's theory. Pioneering work is proposed by Francfort and Marigo (Francfort and Marigo, 1998), and then Bourdin et al. set forth a regularized version that can be solved numerically (Bourdin et al., 2000; Bourdin et al., 2008). Thenceforth, fruitful research has sprung up, facilitating the sustaining perfection of PFM (Ambati et al., 2016; Li and Maurini, 2019; Miehe et al., 2010b; Wu and Nguyen, 2018). Despite the vast majority of studies concentrate on brittle fracture with small deformations, some extensions to nonlinear elasticity are of great significance (Borden et al., 2016; Hesch and Weinberg, 2014; Li and Bouklas, 2020; Miehe and Schänzel, 2014; Tang et al., 2019). For instance, in the general framework of finite deformations, Miehe et al. first constructed a phase field format for the fracture of rubber-like materials with nonlinear constitutive properties (Miehe and Schänzel, 2014). On this basis, Loew et al. proposed a rate-dependent PFM and verified it experimentally (Loew et al., 2019). Recently, Shen et al. and Yin et al. further extended it to more complex viscoelastic systems (Shen et al., 2019; Yin and Kaliske, 2020). Note that the existing investigations basically cover materials with various mechanical responses (Ambati et al., 2015; Shen et al., 2019; Wu et al., 2016; Zhang et al., 2019), demonstrating the universality of the phase field method is unquestioned. To our knowledge, however, the vast majority of previous reports on phase field modeling of fracture involving nonlinear deformation are limited to quasi-static. At least in the mechanics community, research related to the coupling of phase field modeling and nonlinear elastic dynamics is almost blank (except for a blast study based on IGA–RKPM (Moutsanidis et al., 2018)). Breakthroughs in this respect have germinated in the physics community. Chen and his colleagues proposed a modified physics-based PFM to fill this gap (Chen et al., 2017; Lubomirsky et al., 2018). Using large-scale

finite-difference simulations ($\sim 10^7$ grid nodes), they unprecedentedly reproduced the crack oscillation instability observed in the experiments. Nonetheless, the simulations they showed will lead to burdensome computational efforts.

This study is dedicated to accomplishing the phase field modeling of high-speed crack instability in the rapid fracture of hyperelastic materials. The direct extension of the mechanical-based phase field model that excels in brittle fracture to nonlinear dynamic fracture was discovered to be unworkable. Enlightened by recent physics-based PFM (Chen et al., 2017), a novel dynamic PFM with no attenuation of wave speed that roots in Griffith's theory was derived based on the nonconservative Lagrange's equation. However, our experience indicates that this model requires special tricks to address the mesh distortion in large deformation rapid fractures (Tian et al., 2019a). To this end, we developed a crucial adaptive distorted mesh removal scheme (ADMR). Moreover, an excellent multi-level hybrid adaptive mesh algorithm is implemented to speed up computing (Tian et al., 2019b). The detailed numerical implementation via the finite element method (FEM) is outlined. Afterward, the reliability of the model as well as the internal code is testified by two quasi-static fracture benchmarks. On the strength of the fresh model and algorithms, ultra-high-speed crack oscillation and tip-splitting instabilities beyond the capabilities of the classical mechanical-based model were successfully replicated, in good agreement with experimental observations (Livne et al., 2007; Lubomirsky et al., 2018). The origin of the discrepancies between the novel and conventional models is also briefly explored.

The remainder of this article is organized as follows. Section 2 lays a solid theoretical foundation for the energy formulation of the novel rate-dependent dynamic phase field model in non-linear deformation systems. Strong form governing equations are derived per the nonconservative Lagrangian equation. In Section 3, we outline the detailed numerical implementations using FEM. The key algorithms therein are demonstrated in the form of pseudo-code. Section 4 aims to verify the reliability of the new model and algorithm through two previously reported quasi-static fracture tests. In Section 5, a comparative study of the proposed and the traditional models were conducted using a pre-strained fracture configuration. At last, the salient conclusions are summarized in Section 6.

2. Theoretical aspects of phase field modeling

2.1. Phase-field approximation of diffuse cracks

The crucial idea of the phase-field modeling of fracture lies in regularizing the sharp crack topology within a bounded diffuse damage band. Let us consider a hyperelastic body with the initial configuration $\Omega \subset \mathbb{R}^n$ ($n = 2, 3$), enclosed by the surface $\partial\Omega \subset \mathbb{R}^{n-1}$, as depicted in Fig. 1(a). During the deformation process,
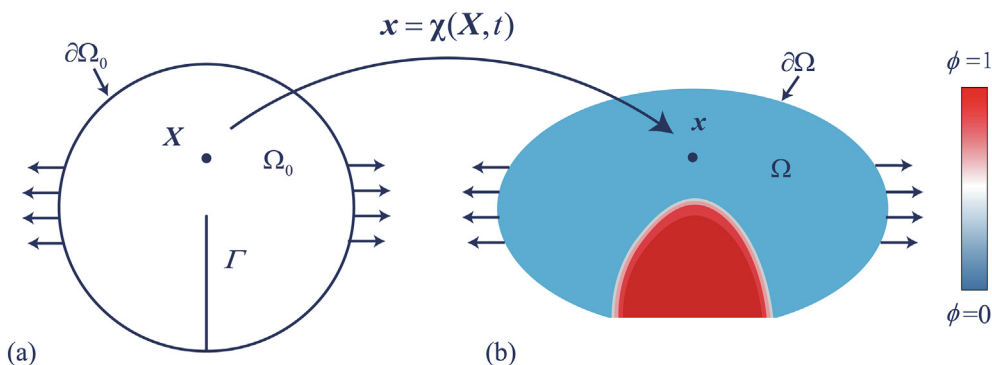

Fig. 1. (a) Schematic of an elastomer containing internal discontinuity surfaces Γ in its initial configuration. (b) Phase field description of discrete cracks in the current configuration.

the internal discontinuous surfaces Γ are regularized by introducing an auxiliary phase-field damage variable $\phi(\boldsymbol{X}, t) \in [0, 1]$(see Fig. 1 (b)). The material point X in the initial configuration can be mapped to a new position X in the current deformation configuration by $\boldsymbol{x} = \chi(\boldsymbol{X}, t)$. Then the deformation gradient tensor **F** can be written as

$$\boldsymbol{F} = \nabla_{\boldsymbol{X}} \chi(\boldsymbol{X}, t) = \boldsymbol{I} + \nabla_{\boldsymbol{X}} \boldsymbol{u}, \tag{1}$$

and the Green-Lagrange strain tensor is defined by

$$\boldsymbol{E} = \frac{1}{2}\left(\boldsymbol{F}^T \boldsymbol{F} - \boldsymbol{I}\right), \tag{2}$$

where **I** denotes a second-order unity tensor and **u** represents the displacement field.

In the framework of variational phase-field theory, $\phi = 0$ indicates the pristine state and $\phi = 1$ represents the fully damaged state of the material. The crack surface energy is regularized via

$$\Gamma_l(\phi) = \int_{\Gamma} G_c \mathrm{d}A \approx \int_{\Omega} G_c \gamma(\phi, \nabla\phi) \mathrm{d}V, \tag{3}$$

thereby circumventing the cumbersome discontinuous surface integral (Bourdin et al., 2008). Herein, G_c is the critical energy release of materials and γ is the crack surface density function. Without loss of generality, a representative format of such functions denoted by

$$\gamma(\phi, \nabla\phi) = \frac{1}{4c_w}\left(\frac{w(\phi)}{l_0} + l_0|\nabla\phi|^2\right) \text{ with } c_w = \int_0^1 \sqrt{w(\alpha)}d\alpha \tag{4}$$

is considered (Tanné et al., 2018). Herein, l_0 is a regularization length scale, relying on the inherent material's characteristic length l_{ch}. In particular, we consider the specific format

$$\gamma(\phi, \nabla\phi) = \frac{3}{8}\left(\frac{\phi}{l_0} + l_0|\nabla\phi|^2\right) \tag{5}$$

introduced by (Bourdin et al., 2014) throughout the current work. This model is characterized by predicting the purely linear elasticity stage without damage.

2.2. Nonconservative Lagrangian formulation of dynamic fracture

In the rapid fracture of non-linear elastic materials such as rubber-like polymers, complex dissipative and non-linear deformation occur in the vicinity of the crack tip, i.e. the progress zone (Bouchbinder et al., 2014). In addition to generating new crack surfaces, a small amount of energy is dissipated in the form of heat generation (Sharon et al., 1996). For such a non-conservative system (involving dissipation), its dynamic evolution follows the general form of the Lagrange's equation containing non-conservative forces, that is

$$\frac{d}{dt}\left(\frac{\delta L}{\delta \dot{q}}\right) - \frac{\delta L}{\delta q} + \frac{\delta \mathscr{D}}{\delta \dot{q}} = Q^*, \tag{6}$$

where Lagrangian $L = T - \Pi$, generalized variable $q = (\boldsymbol{u}, \phi)$, D is a dissipation functional and Q^* represents non-conservative forces. The specific formats of the above components are subsequently derived.

2.2.1. Kinetic energy

Inspired by the work of Chen et al. (Chen et al., 2017), we consider the kinetic energy T in the following format

$$T = \frac{\rho_0}{2} \int_{\Omega_0} f(\phi)\dot{\boldsymbol{u}} \cdot \dot{\boldsymbol{u}} \ \mathrm{d}V \tag{7}$$

with

$$\begin{cases} f(\phi) = 1 & (M) \\ f(\phi) = (1 - \phi)^2 + k & (P) \end{cases}. \tag{8}$$

As a result, the change rate of the kinetic energy is derived as

$$\frac{dT}{dt} = \int_{\Omega_0} \left(\rho_0 f(\phi)\ddot{\boldsymbol{u}} + \rho_0 \frac{\partial f(\phi)}{\partial t}\dot{\boldsymbol{u}}\right) \cdot \dot{\boldsymbol{u}}\mathrm{d}V, \tag{9}$$

where ρ_0 is the density at the initial configuration and $\ddot{\boldsymbol{u}}$ is the acceleration vector. A non-negative number k ($0 \leqslant k << 1$) is added for numerical stability purposes ($k \approx 1 \times 10^{-6}$ in this work). Note that the kinetic energy indicated as model P is not independent of phase field damage variables, which is unlike previous dynamic phase field models (model M). And besides, the ensuing investigations also demonstrate striking differences between the above two models.

2.2.2. Potential energy

From the perspective of the variational phase field idea, the total potential energy functional Π can be expressed as the sum of the stored elastic energy and the crack surface energy

$$\begin{aligned} \Pi(\boldsymbol{u}, \phi) &= \int_{\Omega_0 \backslash \Gamma} \psi(\boldsymbol{F})\mathrm{d}V + \int_{\Gamma} G_c \mathrm{d}A \\ &= \int_{\Omega_0} g(\phi)\psi(\boldsymbol{F})\mathrm{d}V + \int_{\Omega_0} G_c \gamma(\phi, \nabla\phi)\mathrm{d}V \end{aligned} \tag{10}$$

in which a monotonically decreasing function $g(\phi) = (1 - \phi)^2 + k$ with $\phi \in [0, 1]$ is introduced to control the degradation of the stored strained energy. For the hyperelastic materials such as polyacrylamide gels, we focus on an experimentally verified plane-stress Neo-Hookean energy functional (Livnet et al., 2010; Livne et al., 2005)

$$\psi(\boldsymbol{F}) = \frac{\mu}{2}\left[\mathrm{tr}\left[\boldsymbol{F}^T \boldsymbol{F}\right] + \det(\boldsymbol{F})^{-2} - 3\right]. \tag{11}$$

Thereupon the variation of the total potential energy functional $\Pi(\boldsymbol{u}, \phi)$ in terms of $\boldsymbol{u}, \phi$ reads

$$\begin{aligned} \delta\Pi(\boldsymbol{u}, \phi, \delta\boldsymbol{u}, \delta\phi) &= \int_{\Omega_0} \left(g(\phi)\frac{\partial\psi(\boldsymbol{F})}{\partial\boldsymbol{F}} : \nabla\delta\boldsymbol{u} + \frac{\partial g(\phi)}{\partial\phi}\psi(\boldsymbol{F})\delta\phi\right)\mathrm{d}V \\ &+ \int_{\Omega_0} \frac{3}{8}G_C\left(\frac{1}{l_0}\delta\phi + 2l_0\nabla\phi \cdot \nabla\delta\phi\right)\mathrm{d}V. \end{aligned} \tag{12}$$

After performing integration by parts, Eq. (12) can be rewritten as

$$\begin{aligned} \delta\Pi(\boldsymbol{u}, \phi, \delta\boldsymbol{u}, \delta\phi) &= - \int_{\Omega_0} (\nabla_{\boldsymbol{X}} \cdot \boldsymbol{P}) \cdot \delta\boldsymbol{u}\mathrm{d}V + \int_{\partial\Omega_0} (\boldsymbol{P} \cdot \boldsymbol{n}) \cdot \delta\boldsymbol{u}\mathrm{d}A \\ &+ \int_{\Omega_0} \left(\frac{\partial g(\phi)}{\partial\phi}\psi(\boldsymbol{F}) + \frac{3}{8}\left(\frac{G_c}{l_0} - 2G_c l_0\nabla^2\phi\right)\right)\delta\phi\mathrm{d}V \\ &+ \int_{\partial\Omega_0} \frac{3}{4}G_c l_0\nabla_{\boldsymbol{X}}\phi \cdot \boldsymbol{n}_0\delta\phi\mathrm{d}A \end{aligned} \tag{13}$$

where the first Piola–Kirchhoff stress (PK1) defined by

$$\begin{aligned} \boldsymbol{P} &= g(\phi)\frac{\partial\psi(\boldsymbol{F})}{\partial\boldsymbol{F}} \\ &= \left((1 - \phi)^2 + k\right)\mu\left[\boldsymbol{F} - \det(\boldsymbol{F})^{-2}\boldsymbol{F}^{-T}\right] \end{aligned} \tag{14}$$

is introduced. To facilitate numerical implementation, we also derive the second Piola-Kirchhoff stress (PK2)

$$\boldsymbol{S} = \boldsymbol{F}^{-1} \cdot \boldsymbol{P} = \left((1 - \phi)^2 + k\right)\mu\left(\boldsymbol{I} - J^{-2}\boldsymbol{C}^{-1}\right) \tag{15}$$

and the fourth-order elastic tensor

$$\mathbb{C}^{SE} = 2\frac{\partial\boldsymbol{S}}{\partial\boldsymbol{C}} = \left((1 - \phi)^2 + k\right)\left(\mu J^{-2}\left[C_{il}^{-1}C_{kj}^{-1} + C_{ik}^{-1}C_{jl}^{-1}\right] + 2\mu J^{-2}C_{ij}^{-1}C_{kl}^{-1}\right) \tag{16}$$

with the right Cauchy-Green tensor $\boldsymbol{C} = \boldsymbol{F}^T\boldsymbol{F}$ and Jacobian determinant $J = \det(\boldsymbol{F})$.

2.2.3. Dissipation energy

To address non-conservative issues, a well-known Rayleigh dissipation function $\mathscr{D}$ is introduced (Chen et al., 2017; Miehe and Schänzel, 2014; Wu and Nguyen, 2018), which reads

$$\mathscr{D} = \frac{1}{2}\int_{\Omega_0} \eta\dot{\phi}^2 \mathrm{d}V \geqslant 0. \tag{17}$$

Here, $\eta \geqslant 0$ (unit : $\mathrm{Nm}^{-2}\cdot \mathrm{s}$) is the viscosity coefficient responsible for the rate-dependent fracture and regulates the rate of energy dissipation, equating to Ginzburg-Landau dynamics for phase field. Following the derivation of (Chen et al., 2017) and (Mesgarnejad et al., 2019), the determination of η value in the current work follows

$$\eta = \beta\frac{G_C}{2c_w V_S} \tag{18}$$

where β is a dimensionless parameter. Our numerical tests indicate that the smaller β delays the occurrence of instability. Given the point of the current work, we directly set β as 0.28, in line with (Chen et al., 2017). Incidentally, apart from explicitly satisfying the second law of thermodynamics (Chen et al., 2017), the introduction of Eq. (17) also improves the robustness of the numerical calculation.

2.2.4. Externally applied energy

In the general case, the externally applied energy $\mathscr{P}^{\mathrm{ext}}$ can be straightforwardly written as

$$\mathscr{P}^{\mathrm{ext}} = \int_{\Omega}\bar{\mathbf{b}}_0\cdot\mathbf{u}\mathrm{d}V + \int_{\partial\Omega}\bar{\mathbf{t}}_0\cdot\mathbf{u}\mathrm{d}A, \tag{19}$$

where $\bar{\boldsymbol{b}}_0$ and $\bar{\boldsymbol{t}}_0$ are the body and traction force vectors, respectively. The variation of Eq. (19) is derived as

$$\delta\mathscr{P}^{\mathrm{ext}} = \int_{\Omega}\bar{\mathbf{b}}_0\cdot\delta\mathbf{u}\mathrm{d}V + \int_{\partial\Omega}\bar{\mathbf{t}}_0\cdot\delta\mathbf{u}\mathrm{d}A, \tag{20}$$

corresponding to the non-conservative forces Q^* in the Lagrange equation (Eq. (6)).

2.3. Governing equations

Considering the independence of $\delta\boldsymbol{u}$ and $\delta\phi$, we derived the following equilibrium equations from Eqs. (6), (9), (13), (17) and (20), that is

$$\int_{\Omega_0}\left(\rho_0 f(\phi)\ddot{\boldsymbol{u}} + \rho_0\frac{\partial f(\phi)}{\partial t}\dot{\boldsymbol{u}} - \nabla_X\cdot\boldsymbol{P} - \bar{\boldsymbol{b}}_0\right)\cdot\delta\boldsymbol{u}\mathrm{d}V$$
$$+ \int_{\partial\Omega_0}\left(\boldsymbol{P}\cdot\boldsymbol{n} - \bar{\boldsymbol{t}}_0\right)\cdot\delta\boldsymbol{u}\mathrm{d}A = 0 \tag{21}$$

and

$$\int_{\Omega_0}\left(\frac{\partial g(\phi)}{\partial\phi}\psi(\boldsymbol{F}) + \frac{3}{8}\left(\frac{G_c}{l_0} - 2G_c l_0\nabla^2\phi\right) + \eta\dot{\phi} - \frac{\rho_0}{2}\frac{\partial f(\phi)}{\partial\phi}\dot{\boldsymbol{u}}\cdot\dot{\boldsymbol{u}}\right)\delta\phi\mathrm{d}V$$
$$+ \int_{\partial\Omega_0}\frac{3}{4}G_c l_0\nabla_X\phi\cdot\boldsymbol{n}_0\delta\phi\mathrm{d}A = 0. \tag{22}$$

With the randomicity of $\delta\boldsymbol{u}$ and $\delta\phi$ in mind, Eqs. (21) and (22) yield the governing equations of mechanical response and phase field evolution

$$\begin{cases} \rho_0 f(\phi)\ddot{\boldsymbol{u}} + \rho_0\frac{\partial f(\phi)}{\partial t}\dot{\boldsymbol{u}} = \nabla_X\cdot\boldsymbol{P} + \bar{\boldsymbol{b}}_0 \\ \frac{3}{8}\left(\frac{G_c}{l_0} - 2G_c l_0\nabla^2\phi\right) + \eta\dot{\phi} - \frac{\rho_0}{2}\frac{\partial f(\phi)}{\partial\phi}\dot{\boldsymbol{u}}\cdot\dot{\boldsymbol{u}} = 2(1-\phi)\psi(\boldsymbol{F}) \\ \boldsymbol{P}\cdot\boldsymbol{n} = \bar{\boldsymbol{t}}_0 \quad \text{at } \partial\Omega_0 \\ \nabla_X\phi\cdot\boldsymbol{n}_0 = 0 \quad \text{at } \partial\Omega_0 \end{cases} \tag{23}$$

Herein, $f(\phi)$ has several alternative formats. Nevertheless, this contribution only considers two different models presented in Eq. (8), i.e., models M and P.

3. Numerical implementation

3.1. Weak form

The governing equations summarized in Eq. (23) can be solved numerically via the finite element method (FEM). Following the Galerkin weighted residual method and utilizing integration by parts, the weak form of mechanical response reads

$$\boldsymbol{R_u} = \int_{\Omega_0}\left(\rho_0 f(\phi)\ddot{\boldsymbol{u}} + \rho_0\frac{\partial f(\phi)}{\partial t}\dot{\boldsymbol{u}}\right)\cdot\delta\boldsymbol{u}\mathrm{d}V + \int_{\Omega_0}\boldsymbol{P}:\nabla_X\delta\boldsymbol{u}\mathrm{d}V$$
$$- \int_{\Omega_0}\bar{\boldsymbol{b}}\cdot\delta\boldsymbol{u}\mathrm{d}V - \int_{\Gamma_N}\bar{\boldsymbol{t}}\cdot\delta\boldsymbol{u}\mathrm{d}A = 0 \quad \forall\delta\boldsymbol{u}\in\mathscr{V}_{\mathrm{u}} \tag{24}$$

Likewise, the weak form of phase field evolution is derived as

$$\boldsymbol{R_\phi} = \int_{\Omega_0}\left(\frac{3}{4}G_c l_0\nabla_X\phi\cdot\nabla_X\delta\phi + \frac{3}{8}\frac{G_c}{l_0}\delta\phi + \eta\dot{\phi}\delta\phi\right)\mathrm{d}V$$
$$- \int_{\Omega_0}2(1-\phi)\psi(\boldsymbol{F})\delta\phi\mathrm{d}V - \int_{\Omega_0}\frac{\rho_0}{2}\frac{\partial f(\phi)}{\partial\phi}\dot{\boldsymbol{u}}\cdot\dot{\boldsymbol{u}}\delta\phi\mathrm{d}V = 0 \quad \forall\delta\phi\in\mathscr{V}_\phi \tag{25}$$

Here, $\mathscr{V}_{\mathrm{u}}$ and $\mathscr{V}_\phi$ are trial spaces for displacement field $\boldsymbol{u}$ and phase-field ϕ, which follows

$$\begin{cases} \mathscr{V}_{\mathrm{u}} = \{\delta\mathbf{u}|\delta\mathbf{u} = \mathbf{0} \text{ on } \partial\Omega_0\} \\ \mathscr{V}_\phi = \{\delta\phi|\delta\phi = 0 \text{ on } \Gamma_C\} \end{cases} \tag{26}$$

In consideration of the quasi-static fracture problem involved in the subsequent examples, the corresponding weak forms are reduced by Eqs. (24) and (25), yielding

$$\begin{cases} \boldsymbol{R_u^s} = \int_{\Omega_0}\boldsymbol{P}:\nabla_X\delta\boldsymbol{u}\mathrm{d}V - \int_{\Omega_0}\bar{\boldsymbol{b}}\cdot\delta\boldsymbol{u}\mathrm{d}V - \int_{\Gamma_N}\bar{\boldsymbol{t}}\cdot\delta\boldsymbol{u}\mathrm{d}A = 0 \\ \boldsymbol{R_\phi^s} = \int_{\Omega_0}-2(1-\phi)\psi(\boldsymbol{F})\delta\phi\mathrm{d}V + \int_{\Omega_0}\left(\frac{3}{8}\frac{G_c}{l_0}\left(l_0^2\nabla_X\phi\cdot\nabla_X\delta\phi + \delta\phi\right) + \eta\dot{\phi}\delta\phi\right)\mathrm{d}V = 0 \end{cases}. \tag{27}$$

The function $f(\phi)$ vanishes in Eq. (27), signifying that models P and M are identical in terms of quasi-static.

3.2. Spatial and temporal discretization

As mentioned earlier, Classical FEM is used to discretize the fundamental field variables $\boldsymbol{u}$, ϕ and their gradients in space, as follows

$$\boldsymbol{u} = \sum_{i=1}^m\boldsymbol{N}_i^u\boldsymbol{u}_i, \quad \phi = \sum_{i=1}^m N_i\phi_i, \quad \boldsymbol{\varepsilon} = \nabla\boldsymbol{u} = \sum_{i=1}^m\boldsymbol{B}_i^u\boldsymbol{u}_i, \quad \nabla\phi = \sum_{i=1}^m\boldsymbol{B}_i^\phi\phi_i \tag{28}$$

with

$$\boldsymbol{N}_i^u = \begin{bmatrix} N_i & 0 \\ 0 & N_i \end{bmatrix}, \quad \boldsymbol{B}_i^u = \begin{bmatrix} N_{i,x} & 0 \\ 0 & N_{i,y} \\ N_{i,y} & N_{i,x} \end{bmatrix}, \quad \boldsymbol{B}_i^\phi = \begin{bmatrix} N_{i,x} \\ N_{i,y} \end{bmatrix}. \tag{29}$$

where, N_i and m denote the shape function of the T3 (Q4) element and its nodal number, respectively.

In light of the temporal discretization required for dynamic problems, an explicit velocity Verlet algorithm (Swope et al., 1982)

$$\begin{cases} \boldsymbol{u}_{n+1} = \boldsymbol{u}_n + \dot{\boldsymbol{u}}_n\Delta t + \frac{1}{2}\ddot{\boldsymbol{u}}_n\Delta t^2 \\ \dot{\boldsymbol{u}}_{n+1} = \dot{\boldsymbol{u}}_n + \frac{\ddot{\boldsymbol{u}}_n + \ddot{\boldsymbol{u}}_{n+1}}{2}\Delta t \end{cases} \tag{30}$$

is utilized. The time step Δt is limit by the Courant-Friedrichs-Lewy (CFL) condition

$$\Delta t < \Delta t_{CFL} = h_{\min}/V_R \tag{31}$$

to meet condition stability (Li et al., 2016). Here $h_{\min}$ is the minimum of element size, and V_R is the Rayleigh wave velocity of the

material. Remarkably, $h_{\min}$ may drastically decrease as the deformation intensifies. For this reason, we chose a fairly small-time increment, approximately $0.01\Delta t_{CFL}$. Besides, concerning the dissipative item, we adopt a backward Euler difference method

$$\dot{\phi} = \frac{\phi_{n+1} - \phi_n}{\Delta t}, \tag{32}$$

where $\phi_n \ (\phi_{n+1})$ represents the damage phase field at the time $t_n \ (t_{n+1})$.

3.3. Linearization

Let us start with the quasi-static case (i.e., neglecting kinetic energy). Using the Newton-Raphson method to linearize Eq. (27), we thus obtain

$$\begin{bmatrix} \boldsymbol{K}_{uu}^s & \boldsymbol{K}_{u\phi}^s \\ \boldsymbol{K}_{\phi u}^s & \boldsymbol{K}_{\phi\phi}^s \end{bmatrix} \begin{Bmatrix} \Delta\boldsymbol{u} \\ \Delta\phi \end{Bmatrix} = \begin{Bmatrix} \boldsymbol{f}_u^s \\ \boldsymbol{f}_\phi^s \end{Bmatrix}. \tag{33}$$

With the discretization in mind, the residual vectors $\boldsymbol{f}_u^s$ and $\boldsymbol{f}_\phi^s$ are written as

$$\begin{cases} \boldsymbol{f}_u^s = -\int_{\Omega_0} \boldsymbol{B}_X^T \{\boldsymbol{S}\} dV + \int_{\Omega_0} N\bar{\boldsymbol{b}} dV + \int_{\Gamma_N} N\bar{\boldsymbol{t}} dA \\ \boldsymbol{f}_\phi^s = \int_{\Omega_0} \left[2N_\phi\psi(\boldsymbol{F})(1-\phi_{n+1}) - \frac{3}{4}\boldsymbol{B}_\phi^T G_c l_0 \boldsymbol{B}_\phi \phi_{n+1} - \frac{3}{8} G_c l_0 N_\phi - \frac{\eta}{\Delta t} N_\phi(\phi_{n+1}-\phi_n) \right] dV \end{cases} \tag{34}$$

and the tangent stiffness matrices $\boldsymbol{K}_{uu}^s, \boldsymbol{K}_{u\phi}^s, \boldsymbol{K}_{\phi u}^s$ and $\boldsymbol{K}_{\phi\phi}^s$ are given by

$$\begin{cases} \boldsymbol{K}_{uu}^s = \frac{\partial R_u^s}{\partial \boldsymbol{u}} = \int_{\Omega_0} \boldsymbol{B}_X^T \mathbb{C} \boldsymbol{B}_X dV + \int_{\Omega_k} \mathscr{B}^T \tilde{\boldsymbol{S}} \mathscr{B} dV \\ \boldsymbol{K}_{u\phi}^s = \frac{\partial R_u^s}{\partial \phi} = \int_{\Omega_0} \boldsymbol{B}_X^T \frac{\partial \boldsymbol{S}}{\partial \phi} N_\phi dV \\ \boldsymbol{K}_{\phi u}^s = \frac{\partial R_u^s}{\partial \phi} = \int_{\Omega_0} N_\phi^T \left[\frac{\partial \boldsymbol{S}}{\partial \phi} \right]^T \boldsymbol{B}_X dV \\ \boldsymbol{K}_{\phi\phi}^s = \int_{\Omega_0} \left[2N_\phi\psi(\boldsymbol{F})N_\phi^T + \frac{3}{4}\boldsymbol{B}_\phi^T G_c l_0 \boldsymbol{B}_\phi + \frac{\eta}{\Delta t} N_\phi N_\phi^T \right] dV \end{cases} \tag{35}$$

Herein, $\boldsymbol{B}_X$ and $\mathscr{B}$ are the gradients matrices defined by

$$\boldsymbol{B}_0 = \begin{bmatrix} N_{i,x}F_{11} & N_{i,x}F_{21} \\ N_{i,y}F_{12} & N_{i,y}F_{12} \\ N_{i,x}F_{12}+N_{i,y}F_{11} & N_{i,x}F_{22}+N_{i,y}F_{21} \end{bmatrix}, \quad \mathscr{B} = \begin{bmatrix} N_{i,x} & \boldsymbol{0} \\ N_{i,y} & \boldsymbol{0} \\ \boldsymbol{0} & N_{i,x} \\ \boldsymbol{0} & N_{i,y} \end{bmatrix} \tag{36}$$

Note that, in general, monolithically solving Eq. (33) is an arduous task, thus a staggered (alternating minimization) algorithm proposed by (Miehe et al., 2010a) is implemented, which yields

$$\begin{cases} \boldsymbol{K}_{uu}^s \cdot \Delta\boldsymbol{u} = \boldsymbol{f}_u^s \\ \boldsymbol{K}_{\phi\phi}^s \cdot \Delta\phi = \boldsymbol{f}_\phi^s \end{cases}. \tag{37}$$

Thanks to the decoupling of displacement and damage phase field, this scheme is very robust with a small loading increment.

Whereas for dynamic fractures in the presence of nonlinear deformation, the weak form of motion equation (Eq. (24)) after discretization takes the following explicit form

$$\boldsymbol{M}\ddot{\boldsymbol{u}} = \boldsymbol{f}_{ext} - \boldsymbol{f}_{int}(\boldsymbol{u}, \phi). \tag{38}$$

with $\boldsymbol{M} = \int_{\Omega_0} \rho_0 f(\phi) NN^T dV$ the consistent mass matrix and $\boldsymbol{f}_{ext}$ the external force vector. $\boldsymbol{f}_{int}(\boldsymbol{u}, \phi)$ denotes the internal force vector, which is given explicitly as

$$\boldsymbol{f}_{int} = \int_{\Omega_0} \boldsymbol{B}_X^T \{\boldsymbol{S}\} dV + \int_{\Omega_0} N\rho_0 \frac{\partial f(\phi)}{\partial \phi} \frac{\phi_{n+1}-\phi_n}{\Delta t} \dot{\boldsymbol{u}} dV. \tag{39}$$

Similarly, the format of dynamic damage evolution is derived as

$$\boldsymbol{K}_{\phi\phi} \cdot \Delta\phi = \boldsymbol{f}_\phi \tag{40}$$

with the stiffness matrix

$$\boldsymbol{K}_{\phi\phi} = \int_{\Omega_0} \left(2N_\phi\psi(\boldsymbol{F})N_\phi^T + \frac{3}{4}\boldsymbol{B}_\phi^T G_c l_0 \boldsymbol{B}_\phi + \frac{\eta}{\Delta t} N_\phi N_\phi^T - \frac{\rho_0}{2} \frac{\partial^2 f(\phi)}{\partial\phi^2} \dot{\boldsymbol{u}} \cdot \dot{\boldsymbol{u}} N_\phi N_\phi^T \right) dV \tag{41}$$

and the residual vector

$$\boldsymbol{f}_\phi = \int_{\Omega_0} \left(2N_\phi\psi(\boldsymbol{F})(1-\phi_{n+1}) - \frac{3}{4}\boldsymbol{B}_\phi^T G_c l_0 \boldsymbol{B}_\phi \phi_{n+1} - \frac{3}{8} G_c l_0 N_\phi \right) dV$$
$$- \int_{\Omega_0} \frac{\eta}{\Delta t} N_\phi(\phi_{n+1}-\phi_n) dV + \int_{\Omega_0} N_\phi \frac{\rho_0}{2} \frac{\partial f(\phi)}{\partial\phi} \dot{\boldsymbol{u}} \cdot \dot{\boldsymbol{u}} dV. \tag{42}$$

3.4. Irreversibility constraints

As previously stated, the irreversibility (non-healing nature) of cracks is enforced by constraint inequality

$$\dot{\phi} = \frac{\phi_{n+1} - \phi_n}{\Delta t} \geqslant 0. \tag{43}$$

To accomplish this, an active set method is employed in our simulations (Loew et al., 2019). As per the sign of the phase field increment $\Delta\phi$ within an adjacent time step, we partition the system of equations that govern the damage evaluation into an active set $\mathscr{A} = \{i | \Delta\phi < 0\}$ and its complementary set $\mathscr{A}' = \{i | \Delta\phi \geqslant 0\}$. At each iteration step, we only solve the following reduced systems

$$\Delta\phi_{\mathscr{A}'} = -(\boldsymbol{K}_\phi)_{\mathscr{A}'\mathscr{A}'}^{-1} (\boldsymbol{f}_\phi)_{\mathscr{A}'} \tag{44}$$

with setting $\Delta\phi_A = 0$. The active set $\mathscr{A}$ is continuously updated in each calculation step until the constraint inequality (Eq. (43)) is fulfilled globally. The detailed procedure is depicted by the pseudocode summarized in Algorithm 1.

Algorithm 1 Active set method.
1. $\mathscr{A} = \phi, \mathscr{A}' = \cup$
2. while $\min(\Delta\phi_{\mathscr{A}'}) < 0$ do
3. $\quad \mathscr{A} = \mathscr{A} \cup (\Delta\phi_{\mathscr{A}'} < 0)$
4. $\quad \mathscr{A}' = \cup \{.\mathscr{A}$
5. $\quad \Delta\phi_{\mathscr{A}'}^{n+1} = -\left(\boldsymbol{K}_\phi^{n+1}\right)_{\mathscr{A}'\mathscr{A}'}^{-1} \left(\boldsymbol{f}_\phi^{n+1}\right)_{\mathscr{A}'}$
6. $\quad \Delta\phi_{\mathscr{A}} = 0$
7. end
8. $\phi^{n+1} = \phi^n + \Delta\phi^{n+1}$

3.5. Multi-level hybrid adaptive mesh method

The adaptive mesh method is a favored scheme out of the non-global nature of crack propagation paths (Heister et al., 2015; Patil et al., 2018). A multi-level hybrid adaptive mesh strategy for brittle fracture proposed in our previous work is implemented effortlessly in the framework of finite strains (Tian et al., 2019b). In a nutshell, this approach utilizes multi-level hybrid elements whose levels rest with damage variable to discretize the entire solution domain, eliminating dangling nodes and assuring high isotropy of the mesh in the vicinity of crack tips. The superior performance of the proposed strategy has been testified by several representative quasi-

static and dynamic fracture benchmarks. To clarify, the rudimentary procedure of the adaptive scheme is delineated in Algorithm 2.

Algorithm 2 Multi-level hybrid adaptive mesh strategy

1. Define maximum mesh refinement level $R_{\max}$, the upper threshold for mesh refinement ϕ_R ($0.1 < \phi_R \leqslant 0.25$), lower threshold for mesh coarsening ϕ_c ($0 < \phi_c \leqslant 0.1$).
2. For element j do
3.   If $\phi > \phi_R \& E_{level} < R_{\max}$ do
4.   Refine the element
5.   Map $Node_{old}; Element_{old}; \boldsymbol{u}_{old}; \dot{\boldsymbol{u}}_{old}; \ddot{\boldsymbol{u}}_{old}$ and ϕ_{old} to $Node_{new}; Element_{new}; \boldsymbol{u}_{new}; \dot{\boldsymbol{u}}_{new}; \ddot{\boldsymbol{u}}_{new}$ and ϕ_{new}
6.   End if
7.   End
8.   For element s do
9.   If $\phi < \phi_c \& E_{level} > 0$
10.   Coarsen the element
11.   Repeat step 5
12.   End if
13.   End
14. Re-identify boundary cells and nodes

3.6. Adaptive distorted mesh removal scheme

In the context of material coordinates (Lagrangian description), phase field modeling of the fracture at large deformation using FEM is prone to mesh distortion, especially in rapid fractures concerning dynamics. To radically address this issue, a novel adaptive distorted mesh removal (ADMR) scheme is developed. This idea stems from the fact that mesh distortion always arises on the crack route depicted by the phase field variable $\phi \geqslant \phi_e$. As illustrated in Fig. 2 (a), the elements located in the mesh-eliminated region circumscribed by the contour line ϕ_e are marked. In our experience, the setting $\phi_e \approx 0.98$ can encompass all distortion elements. After removing the flagged elements, the crack opening profile is visualized as delineated in Fig. 2 (b). Notwithstanding this strategy results in a trivial loss of mass (Wu et al., 2018), it is vital to successfully reproduce rapid fractures at large deformations and is also in accord with the physical reality that the crack-traveled region does not contribute to the system, especially for the proposed model P. Besides, the simulation results in this manner also perfectly match those measured by reported experiments (Bouchbinder, 2009a; Livne et al., 2007). Considering the pivotal

role of this scheme in the entire procedure, the detailed flow is outlined in Algorithm 3.

Algorithm 3 Adaptive distorted mesh removal scheme (ADMR)

1. Define n (time step), n_i(number of intervals), m(nodal number of element)
2. If $n/n_i = $ k (k $= 1, 2, 3\ldots$)
3.   For element j do
4.   If $\frac{1}{m}\sum_{i=1}^{m}\phi_i \geqslant \phi_e$
5.   Delete all data of element j
6.   Reconstruct $Node_n; Element_n; \boldsymbol{u}_n; \dot{\boldsymbol{u}}_n; \ddot{\boldsymbol{u}}_n$ and ϕ_n
7.   End if
8.   End
9. End if
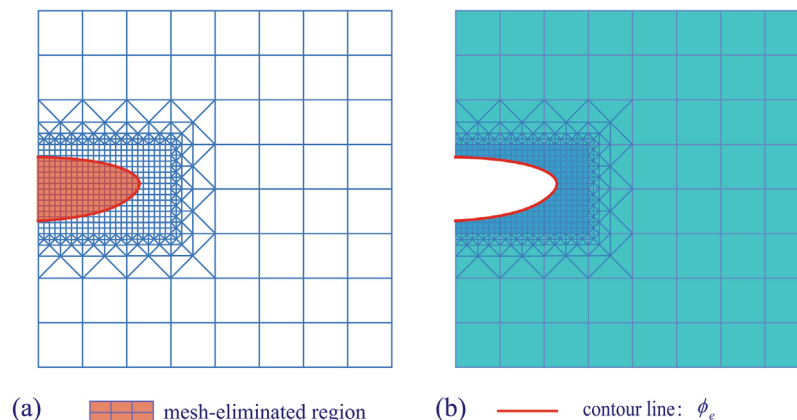10. Re-identify boundary cells and nodes

---

3.7. Solution procedures of pre-strained dynamic fracture

This study is primarily concerned with quasi-static and pre-strained dynamic fractures. The former is straightforward and we have no intention of reiterating. As regards the pre-strained dynamic fracture, the idea is born of previous experimental configurations (Bleyer et al., 2017; Sharon et al., 1995; Sharon et al., 1996). We first stretch a sufficiently thin and intact specimen until the desired strain state is attained. Holding the strained state, an incision is generated in the middle of the edge with a sharp blade. Then, the seed crack grows immediately and propagates at high speed until the sample thoroughly ruptures. From the perspective of the phase field approach to fracture, ideas similar to experiments can be imitated by the following mathematical procedure.

Phase field approach to pre-strained dynamic fracture

1. Discretization using T4 elements with $E_{Level} = 0$.
2. Define material parameters, time integration parameters, and initialize phase field ϕ_0, displacement field $\boldsymbol{u}_0$.
3. Perform quasi-static loading until the specified strain state.
4. Create a seed crack by enforcing Dirichlet boundary condition $\phi_{\mathscr{C}} = 1$;
5. Initialize the velocity field $\dot{\boldsymbol{u}}_0$, acceleration field $\ddot{\boldsymbol{u}}_0$.
6. For each time step $[t_n, t_{n+1}]$, do
6.1   Update $\boldsymbol{u}_{n+1} = \boldsymbol{u}_n + \dot{\boldsymbol{u}}_n\Delta t + \frac{1}{2}\ddot{\boldsymbol{u}}_n\Delta t^2$.
6.2   while $Res \geqslant tol$ do

(a) ▦ mesh-eliminated region   (b) ——— contour line: ϕ_e

Fig. 2. Illustration of the adaptive distorted mesh removal scheme.
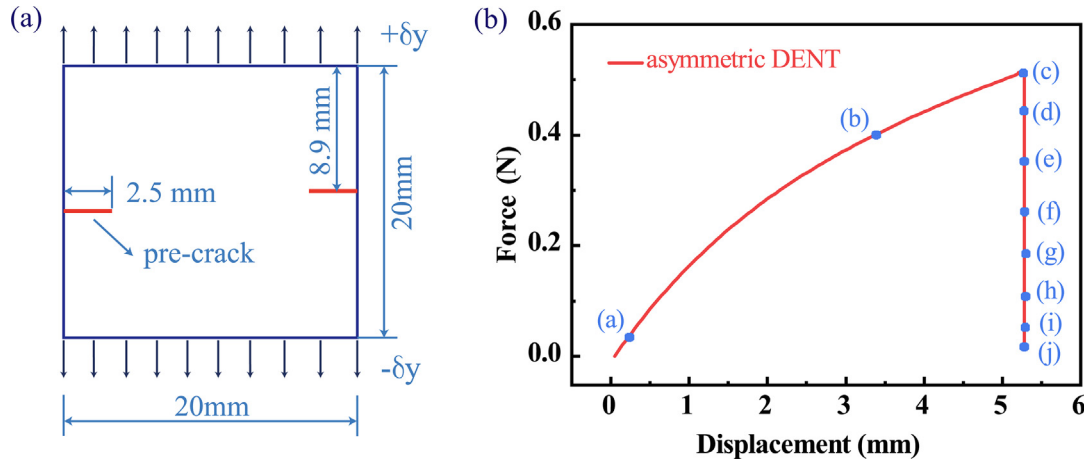
Fig. 3. Asymmetric double-edge-notched tension test. (a). Schematic of the initial geometry and boundary conditions. (b). Force-displacement curve of the test.
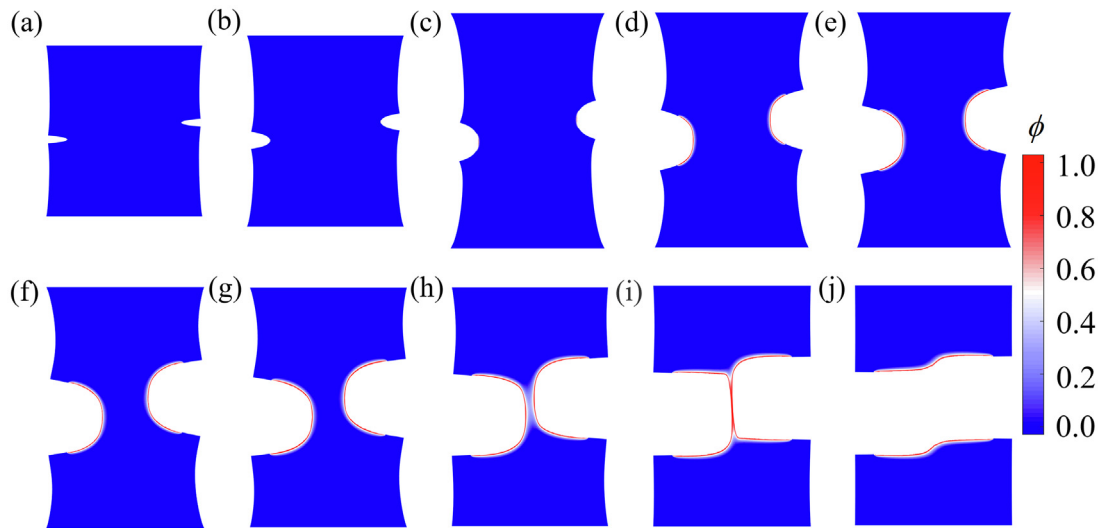

Fig. 4. Snapshots of deformation geometry with crack opening profiles depicted by the contour plot of phase field variables ϕ in different loading states.

Assemble the stiffness matrix $\boldsymbol{K}_{\phi\phi}$ and the residual vector $\boldsymbol{f}_{\phi}$.

Update ϕ_{n+1} according to Algorithm 1.

Define $Res = \frac{\|\boldsymbol{f}_{\phi}^{i+1}\|}{\|\boldsymbol{f}_{\phi}^{i}\|}$ with the Euclidean norm $\|\cdot\|$.

End

6.3 Get the lumped mass matrix $\boldsymbol{M}_{n+1}$, force vector $\boldsymbol{f}_{n+1}$.

6.4 Compute acceleration $\ddot{\boldsymbol{u}}_{n+1} = \boldsymbol{M}_{n+1}^{-1}\boldsymbol{f}_{n+1}$.

6.5 Update velocity $\dot{\boldsymbol{u}}_{n+1} = \dot{\boldsymbol{u}}_{n+1} + \frac{1}{2}\Delta t(\ddot{\boldsymbol{u}}_{n+1} + \ddot{\boldsymbol{u}}_{n})$.

6.6 Run the adaptive mesh module (Algorithm 2).

6.7 Run the ADMR module (Algorithm 3).

6.8 Convert multi-level T3 with $E_{Level} = R_{max}$ to Q4 elements (Tian et al., 2019b).

6.9 Re-identify boundary cells and nodes.

7. Go into the next time step and rerun procedure 6 (6.1–6.9).

8. Data processing and visualization.

The aforementioned procedures are implemented entirely by internal MATLAB-based code. Parallel tools and C ++ Mex files are called to accelerate computing. And all the code for the simulations involved in this article is performed on a workstation with Intel (R) Xeon E5-2680 V3 CPU@2.5 GHz, 24 cores processor and 64 GB RAM.
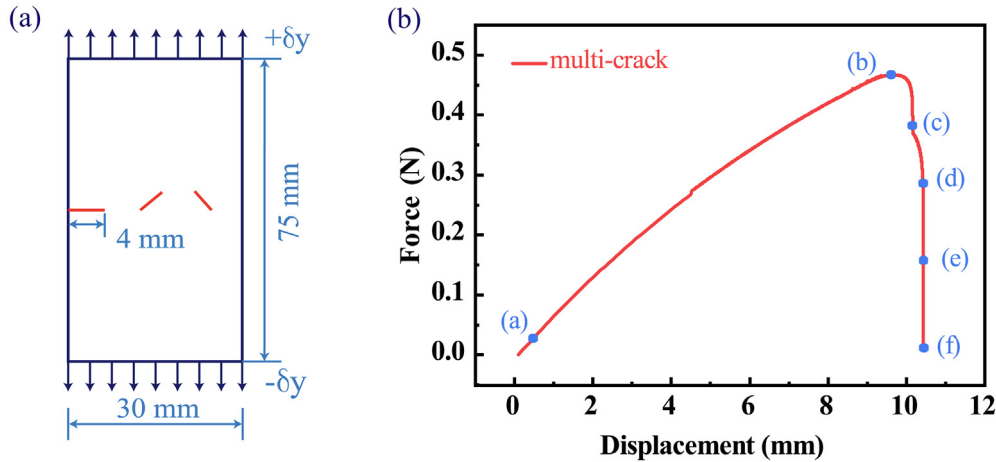
4. Validation via quasi-static tests

In this subsection, we first retested two previously reported quasi-static fracture problems, asymmetric double-edge-notched tension and multi-crack tension tests, to substantiate the validity of the internal code and algorithm.

4.1. The asymmetric double-edge-notched tension (DENT) test

In this example, we consider the quasi-static fracture of an asymmetric double-edge-notched sheet gel specimen under Mode-I loading. The initial geometry (20 mm × 20 mm) and boundary conditions are identical with the settings in (Mao and Anand, 2018), as depicted in Fig. 3 (a). Referring to the work of Fineberg et al. (Livne et al., 2007), The requisite material parameters are set as: $\mu = 0.0352$ N/mm^2 and $G_c = 0.025$ N/mm for the presented Neo-Hookean model. The regularization parameter introduced in phase field theory is set to $l_0 = 0.125$ mm, constraining the mesh size of the adjacent crack path through $h \approx l_0/8$. An adaptive mesh algorithm is conducted to economize computing

Fig. 5. (a). Initial geometry and boundary conditions of multi-crack tension test. (b). The force–displacement curve for this example.
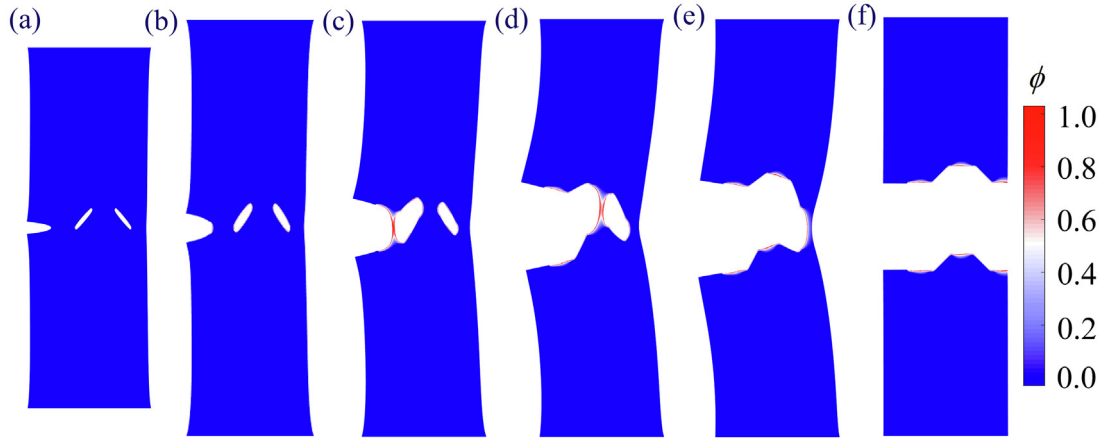

Fig. 6. Crack patterns for the slab containing multiple cracks tension test at loading displacements of $\delta y = 0.5$ mm (a), $\delta y = 9.6463$ mm (b), $\delta y = 10.1593$ mm (c), $\delta y = 10.4206$ mm (d), $\delta y = 10.4301$ mm(f) and $\delta y = 10.4302$ mm (g), respectively.

resources, while viscous dissipation with a nonzero viscosity coefficient $\eta = 1 \times 10^{-3}$ and adaptive loading step scheme are introduced out of numerical stability concerns (Loew et al., 2019). The corresponding force–displacement curve is plotted in Fig. 3 (b). Then, we select several loading states represented by points (a-j) from this graph to display snapshots of their crack patterns. The visualization technique of crack opening profile is by eliminating continuum with the level set of $\phi > 0.8$ in the current configuration. After this post-processing, the crack morphologies are demonstrated in Fig. 4, comprising purely elastic phase (Fig. 4 (a) and (b)), crack initiation (Fig. 4 (c)), growth (Fig. 4 (d)-(e)) and complete fracture (Fig. 4 (f)). The entire evolution course shows a strong resemblance to that reported by Mao et al. (Mao and Anand, 2018) (a complete animation termed S1 is available in the Supplemental Materials).

4.2. Multi-crack tension test

This test involves the merger of multiple cracks, the configuration of which arises from previous experiments and simulations by Loew et al. (Loew et al., 2019). The initial geometry containing three pre-cracks and the imposed boundary conditions are illustrated in Fig. 5 (a). For the sake of simplicity, the constitutive model and material parameters that are completely in accord with the preceding test are used. The regularization parameter for this

example is set to $l_0 = 0.25$ mm, and the mesh size close to the crack route is approximately $l_0/4$ taking advantage of adaptive mesh refinement. Like the previous test, the resulting force–displacement curve is also plotted, as shown in Fig. 5 (b). Subsequently, the crack morphologies at the displacement loading states of $\delta y = 0.5$ mm; $\delta y = 9.6463$ mm; $\delta y = 10.1593$ mm; $\delta y = 10.4206$ mm; $\delta y = 10.4301$ mm and $\delta y = 10.4302$ mm, corresponding to the points (a) through (f) in Fig. 5 (b), are presented in Fig. 6. At first, the specimen undergoes a purely elastic phase, such as Fig. 6 (a). As the loading reaches $\delta y \sim 9.6463$ mm(point b), the crack at the edge initiates. Further stretch the sample with tiny loading increments, the cracks gradually merge and eventually break completely (a complete movie for the crack evolution (S2) is provided in the supplemental materials). Note that the material model used is not consistent with that of the experiment, resulting in larger deformation in this test. Nevertheless, the crack evolution route still matches the experiment well (Loew et al., 2019).

5. Instability in dynamic fracture

After demonstrating the reliability of the algorithms and code, we further investigate the phase field modeling of dynamic fracture instability in hyperelastic gels. In this subsection, the simulation results based on previous (Model M) and novel dynamic
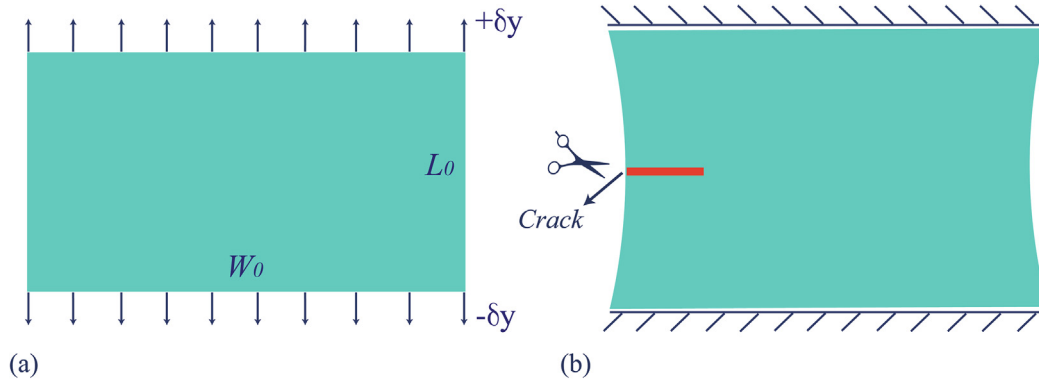
Fig. 7. Schematic of the geometry and applied boundary conditions in the initial (a) and pre-strained states (b).
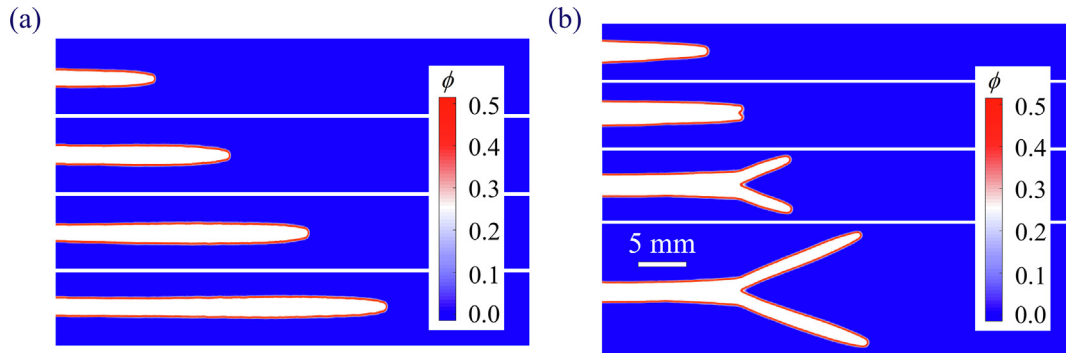

Fig. 8. Crack patterns calculated by the classic dynamic phase field model at pre-strains of $\varepsilon_{yy} = 3.9\%$ and $\varepsilon_{yy} = 5.6\%$, respectively.

fracture models (Model P) are presented and compared with experiments.

5.1. Pre-strained fracture configuration

As stated earlier, this research focuses on the fracture of a pre-strained gel, which has been extensively studied in experiments (Fineberg and Bouchbinder, 2015; Livne et al., 2007; Livne et al., 2010). We consider an intact rectangular specimen with 72 mm width (W_0) and 36 mm height (L_0), as illustrated in Fig. 7 (a). Fixed vertical displacement loads $\pm\delta y$ are applied at the top and bottom edges to hold the total energy of the system constant (see Fig. 7

Fig. 9. Normalized crack propagation velocity V_C/V_S at four different pre-strained states.

(b)). While maintaining this strained state, a seed crack with a length of 7.2 mm is generated by constraining a predefined node set with a phase field value of 1 (fully damage), and then the dynamic fracture is triggered immediately. Drawing on previous findings (Bouchbinder et al., 2014; Chen et al., 2017), the material parameters of the gel are chosen as $\rho = 1290$ Kg/m^3; $\mu = 168 \times 10^3$ Pa; $G_c = 9.6$ J/m^2; $l_0 = 1.5 \times 10^{-4}$ m. The intrinsic shear wave velocity is estimated by $V_S = \sqrt{\mu/\rho} \sim 11.4$ m/s. Remarkably, the aforementioned ADMR algorithm is indispensable for the successful implementation of this simulation.

5.2. Failure of the classical dynamic phase field model

In consideration of the commendations received by the classical dynamic phase field model in linear elastic fracture (Borden et al., 2012; Bourdin et al., 2011), we naturally spread it to nonlinear systems, that is, model M in subsection 2.2.1. Utilizing this model with the material parameters given in the previous subsection, we conducted a series of dynamic fractures at pre-strained states of $\varepsilon_{yy} = 3.9\%$; $\varepsilon_{yy} = 4.4\%$; $\varepsilon_{yy} = 5\%$ and $\varepsilon_{yy} = 5.6\%$, respectively. For the low pre-strained state such as $\varepsilon_{yy} = 3.9\%$, a straight crack propagation path is traced, and the snapshots of its crack patterns at four discontinuously progressive moments are presented in Fig. 8 (a). To visualize the crack opening profile, the mesh that satisfies $\phi > 0.5$ is eliminated in the current configuration (Chen et al., 2017). As the pre-stretched background strain gradually increases, the simple straight cracks are destabilized. As demonstrated in Fig. 8(b), a simple straight crack bifurcates almost symmetrically into two branches at a pre-strain of $\varepsilon_{yy} = 5.6\%$. This phenomenon is not extraordinary in the fracture of hyperelastic gels. Unfortunately, however, the desired crack oscillation instability that has
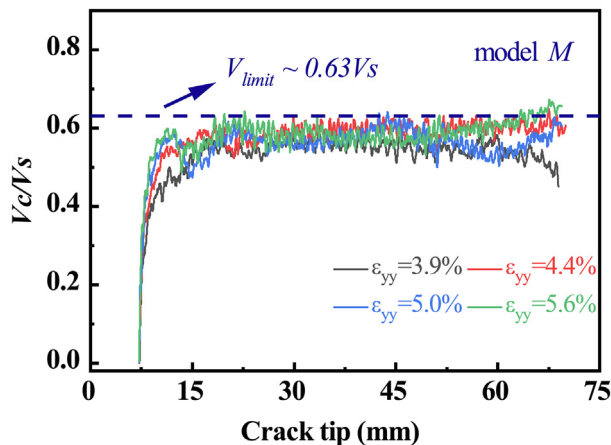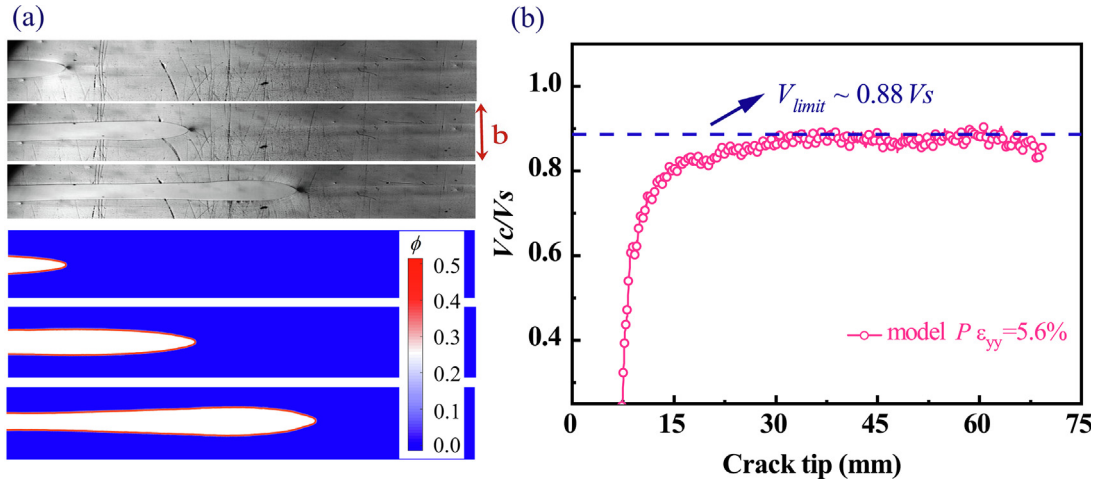
Fig. 10. (a) Comparison of crack patterns predicted from phase field (bottom) and experimental observations (top) at low background strain of $\varepsilon_{yy} = 5.6\%$. (b) The normalized crack velocity V_C/V_S calculated by tracking the advancement of the phase field profile.

been observed in experiments cannot be reproduced in any pre-strained state (Bouchbinder et al., 2014).

After many futile efforts, we are skeptical of the ability of model M to handle dynamic fractures in the framework of non-linear elastic. To ascertain the truth, we measured the crack propagation velocity by tracking the advancement of the phase field profile $\phi = 0.5$. Two-dimensional interpolation was implemented to sketch the phase field contours due to the use of non-uniform adaptive grids, which is realized by simple MATLAB code. The travel distance of the crack tip within a time step $[t_n, t_{n+1}]$ can be calculated by $\Delta l = \sqrt{(x_{n+1} - x_n)^2 + (y_{n+1} - y_n)^2}$, then the crack propagation velocity reads

$$V_C = \frac{\Delta l}{t_{n+1} - t_n} \tag{45}$$

For the comparability of results, the crack velocity is normalized by the shear wave velocity V_S, as presented in Fig. 9. The crack velocity always undergoes a brief acceleration at first, and then enters into a plateau. With increasing pre-strained loading, the plateau of the crack velocity raises slightly. However, the transient crack propagation speed peak is about 0.63 V_S, which is far below the critical velocity of approximately 0.9 V_S measured in experiments (Bouchbinder, 2009a; Livne et al., 2007). With the serious conflicts between model M-based predictions and experimental measurements in mind, we speculate that the classic dynamic fracture model is incompetent for fracture prediction of nonlinear systems. Meanwhile, it is impending to amend the classic dynamic fracture model.

5.3. Rapid fracture predicted by model P

The novel dynamic phase field model (Model P) used here was born for compensating the shortcomings of the classic Model M in non-linear systems. With the same geometry configuration and material parameters as in the previous section, we re-investigated the pre-strained rapid fracture using the Model P-based dynamic phase field model. By manipulating the strength of the pre-stretch, some intriguing phenomena observed in the experiments, such as crack oscillations and tip-splitting, were smoothly reproduced.

5.3.1. Simple straight crack

Starting tentatively with a pre-strain of $\varepsilon_{yy} = 5.6\%$, a sequence of snapshots of the dynamic crack evolution are presented at the

bottom in Fig. 10 (a). In sharp contrast to the crack branching of Model M exhibited in Fig. 8 (b), the novel Model P in the identical circumstances predicts a simple straight crack propagation. The crack tip profile is initially parabolic and gradually converts into a 'tadpole-like' shape as the crack propagates. Intriguingly, this distinctive crack morphology is exceedingly alike to experimental photographs of (Bouchbinder et al., 2014). (see the top of Fig. 10 (a)). In the parlance of the existing research (Bouchbinder et al., 2014), this phenomenon is attributable to the interaction of the dynamic crack with the reflection of waves from the vertical boundaries. For quantitative comparison with model M, the normalized crack velocity V_C/V_S is calculated and plotted in Fig. 10 (b). As observed, the stored strain energy drives the seed crack to initiate at extremely high accelerations. With the rapid attenuation of the acceleration, the crack velocity tends to stabilize at around $0.88V_S$. This stable speed significantly exceeds 0.63 V_S given by model M and is closer to that of infinite medium (Goldman et al., 2010).

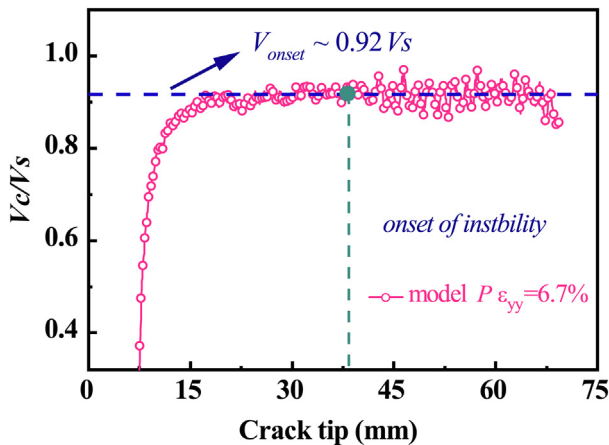#### 5.3.2. Oscillation instability of the crack

With the simple straight crack simulation as the groundwork, we re-perform the same simulation at a higher pre-strained state of $\varepsilon_{yy} = 6.7\%$. As a result, a longing crack oscillation instability was captured, and its time-series photographs are shown in Fig. 11 (a). Immediately after the dynamic fracture was triggered, we first catch sight of simple straight crack propagation with a parabolic crack tip profile. Unlike the low pre-strain case, single straight crack cannot persist for a long time and then sinusoidal path oscillation occurs with a slight increase in amplitude (a complete animation (S3) is provided in the supplemental materials). This oscillation instability with a limited wavelength is particularly fascinating given its purely spontaneous path selection based on the principle of energy minimization. Its oscillatory trait is even more pronounced in the initial configuration (see the top of Fig. 11(a)). For comparative analysis, a series of experimental photographs on crack oscillation instability are invoked from the literature and placed in Fig. 11(b). It is conspicuous that the crack profiles depicted by the model P-based phase field model bear a close resemblance to reality (Chen et al., 2017; Livne et al., 2007), which is unattainable for classical model M. Note, however, that this evidence alone is not sufficient to conclude that Model P is completely reliable.

As uncovered by Fineberg et al. in experiments (Livne et al., 2007), a straight crack starts to destabilize and oscillates in a sinusoidal path at the crack velocity surpasses 0.9 V_S. In light of this,

(a)   (b)
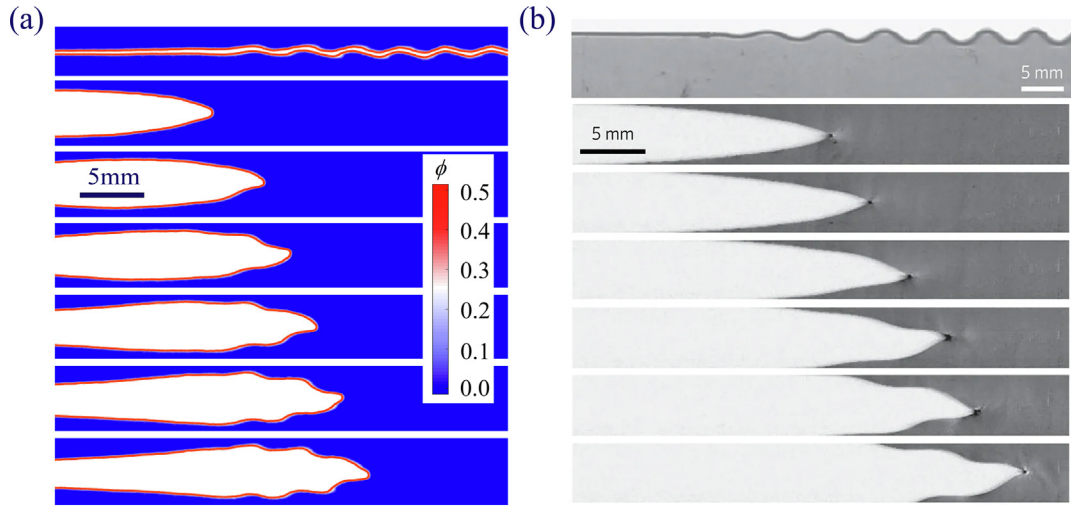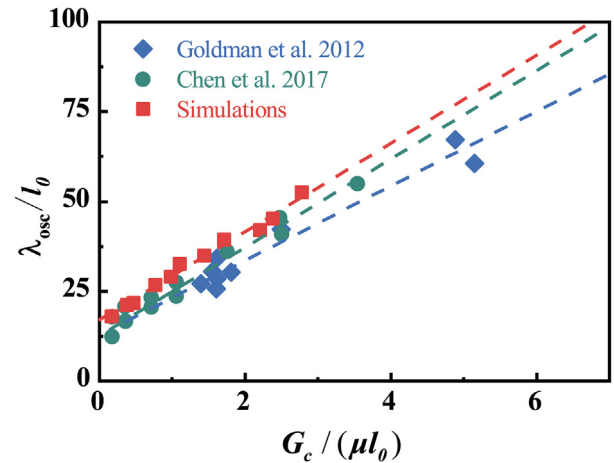

Fig. 11. Comparison of crack oscillation instability reproduced by the Model *P*-based dynamic phase field model (a) with experimental snapshots (b) at pre-strain of $\varepsilon_{yy} = 6.7\%$.

we calculated the normalized crack propagation velocity by tracking the advancement of the phase field outline, as shown in Fig. 12. The crack initiates with higher acceleration on account of the more stored energy compared to the strain state of $\varepsilon_{yy} = 5.6\%$, enabling the crack velocity to uplift to a higher plateau (exceeding $0.9\ V_S$). By precisely locating the crack tip position, we can identify a critical velocity to the onset of the crack oscillation instability $V_{onset} \approx 0.92\ V_S$, quite close to the experimental measurement of $0.9\ V_S$. After the oscillation instability is activated, the crack speed fluctuates immediately, which is also corroborated by experiments (Bouchbinder et al., 2014). To further demonstrate the observed crack oscillations are not a special case, we re-execute the code of this example with different material parameter inputs. By regulating the pre-strained state, the oscillation instability of the crack path has been observed in a series of tests. We measured the oscillation wavelength λ_{osc} and plotted it versus the ratio of the critical elastic energy release rate G_c to the shear modulus μ, as indicated by the red square in Fig. 13. The results demonstrate the oscillation wavelength increases almost linearly with G_c/μ, close to the previous experimental (Goldman et al., 2012) and simulation reports (Chen et al., 2017). Furthermore, we also present the crack patterns and crack speed of another set of material parameter inputs as auxiliary evidence in Appendix A. At this point, we have adequate proofs to endorse that the novel model P is more realistic than


Fig. 13. Evolution of the oscillation wavelength λ_{osc} with G_c/μ scaled by l_0.

the classic dynamic phase field model (model M) in the context of non-linear elastic fracture.

5.3.3. High-speed crack bifurcation

In the foregoing two subsections, the driving force of the crack growth, viz., the stored strain energy per unit area in front of the crack is enhanced by increasing the pre-strain, resulting in a straight-to-oscillation transition of the crack. As such, if we further heighten the driving force, will crack branching emerge? To find out, we perform a series of simulations on the premise that only the pre-strain is alterable. Slightly increasing the pre-strain to $\varepsilon_{yy} = 6.9\ \%$ at first, an awaited tip-splitting (branching) instability emerges immediately following the crack oscillation, as presented in Fig. 14 (a). In the wake of crack branching, the oscillatory instability forthwith vanishes. As the pre-strain is further increased, e.g. $\varepsilon_{yy} = 8.2\ \%$, straight crack directly splits into two symmetrical branches prior to oscillatory instability, as shown in Fig. 14 (b). However, the path oscillations show signs of re-emergence as branch cracks grow, despite only slight traces are currently observed (see the region encircled by the green line in Fig. 14 (b)). Reassuringly, similar phenomena were not only observed in experiments but also reproduced by (Lubomirsky et al., 2018)

Fig. 12. The normalized crack velocity profile V_C/V_S at pre-strain of $\varepsilon_{yy} = 6.7\%$.
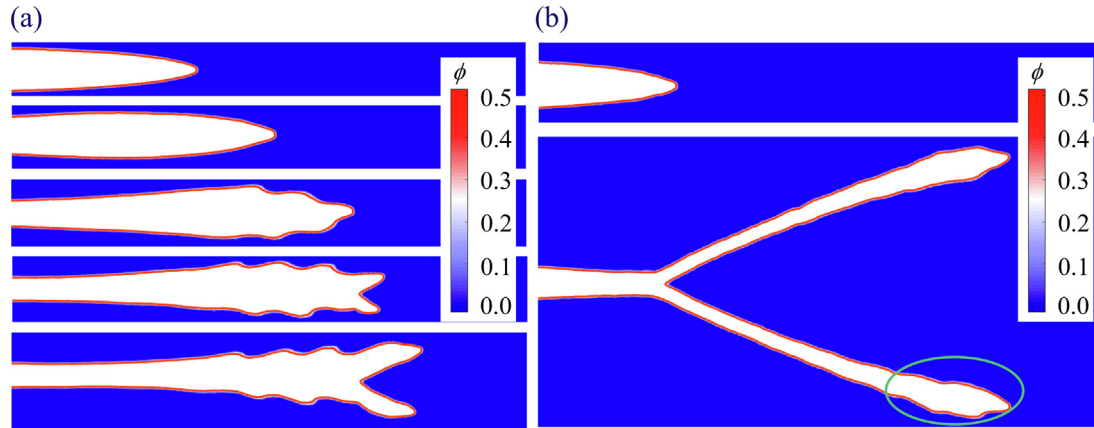
Fig. 14. (a) Transition of the crack path from oscillation to bifurcation at pre-strain of $\varepsilon_{yy} = 6.9\%$. (b) Crack branching without oscillation at pre-strain of $\varepsilon_{yy} = 8.2\%$.

using a physical-based phase field model. The corresponding complete animations (S4 and S5) are provided in the supplemental materials.

In Fig. 15, the normalized crack velocities V_C/V_S corresponding to the crack evolution in Fig. 14 are plotted. The critical velocity of crack tip-splitting instability up to 0.96 V_S was identified, which was slightly beyond the onset speed of crack oscillation ($\sim 0.92\ V_S$). This bifurcation instability breaks the original energy balance, resulting in an instantaneous attenuation in the energy flux into a single branch, thus manifesting a rapid decrease in crack velocity (see Fig. 15). After that, a new equilibrium is gradually established, and oscillation or tip-splitting instability may be triggered again as the crack velocity increases. Superficially, crack instability is closely related to its velocity, however, it intrinsically rests with the driving force of the crack.

5.4. Discrepancies between the two models

The simulation results clearly indicate that the classical model M is no longer valid in nonlinear fracture systems, while the predictions arise from the novel model P closely match the experiments (Bouchbinder et al., 2014; Fineberg and Bouchbinder, 2015; Livne et al., 2007; Lubomirsky et al., 2018). To account for this issue, we recall Eq. (8), the source of the discrepancies between the two models. In general, wave velocity depends on the material parameters, such as the shear wave velocity $V_S = \sqrt{\mu/\rho}$. Since the stiffness degradation due to phase field dam-

age, the shear wave velocity given by model M can be evaluated by $V_S^M = \sqrt{f(\phi)\mu_0/\rho_0}$, which is inconsistent with the fact that the wave velocity in the dissipation zone close to the crack tip remains substantially constant (Chen et al., 2017). In contrast, the more realistic model P predicts $V_S^P = \sqrt{f(\phi)\mu_0/(f(\phi)\rho_0)} = \sqrt{\mu_0/\rho_0}$, independent of the damage. Note that crack propagation requires the energy of the remote medium to be transported to the tip through the elastic waves. Therefore, the wave velocity will inevitably limit the crack velocity (Bouchbinder et al., 2010a). For model M, its ultimate crack velocity is far below the theoretical limit due to the loss of wave velocity (see Fig. 9). Energy accumulation at the crack tip cannot be released by accelerating the crack, leading to unrealistic crack tip splitting (see Fig. 8). Whereas for mode P, thanks to its constant wave velocity nature, ultra-high-speed crack oscillations and bifurcations are smoothly reproduced. However, it should be emphasized that the loss of wave velocity does not seem to elucidate the low-speed crack bifurcations observed in brittle materials (Murphy et al., 2006; Ravi-Chandar, 2004; Ravi-Chandar and Knauss, 1984; Sharon et al., 1995). A complete 3D modeling may be crucial.

6. Conclusion

Based on nonconservative Lagrange's equation, a novel dynamic phase field model termed model P was derived in the framework of non-linear deformation. The distinctive wave velocity invariance of the model P endows its preeminent ability in simulating the rapid fracture of hyperelastic materials. However, the ultra-fine meshes required to identify crack paths as well as the extreme deformation involved in non-linear elastic fractures are daunting tasks for numerical implementation. For this reason, a hybrid adaptive mesh scheme is invoked to save computational overhead while guaranteeing sufficiently fine mesh demands. And besides, an original adaptive distortion mesh removal algorithm was developed to fundamentally address the disruption of the distortion mesh to numerical stability in large deformation fractures. Detailed numerical procedures containing pivotal algorithms are summarized in the context of explicit dynamics, the reliability of which is testified by two quasi-static fracture benchmarks. Utilizing a pre-strained fracture configuration, the intriguing ultra-high-velocity crack oscillations and crack tip splitting instabilities observed in the experiments are successfully reproduced by the novel model P. In contrast, the classical mechanical-based dynamic phase field model named model M encountered failure, indicating that it is unserviceable for non-linear fracture systems. After a comparative analysis, we conclude that the failure of model M originates from
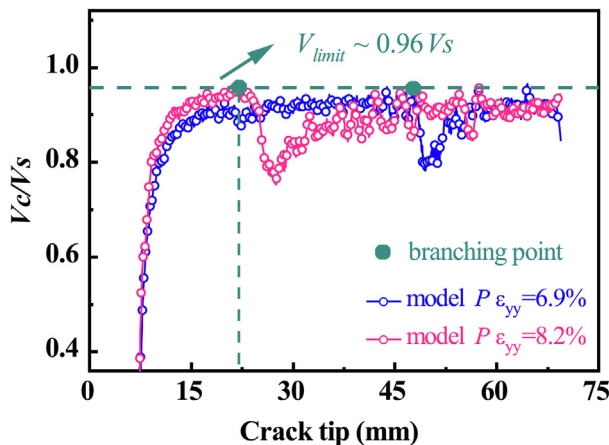
Fig. 15. The normalized crack velocity profiles V_C/V_S at pre-strains of $\varepsilon_{yy} = 6.9\%$ and $\varepsilon_{yy} = 8.2\%$, respectively.
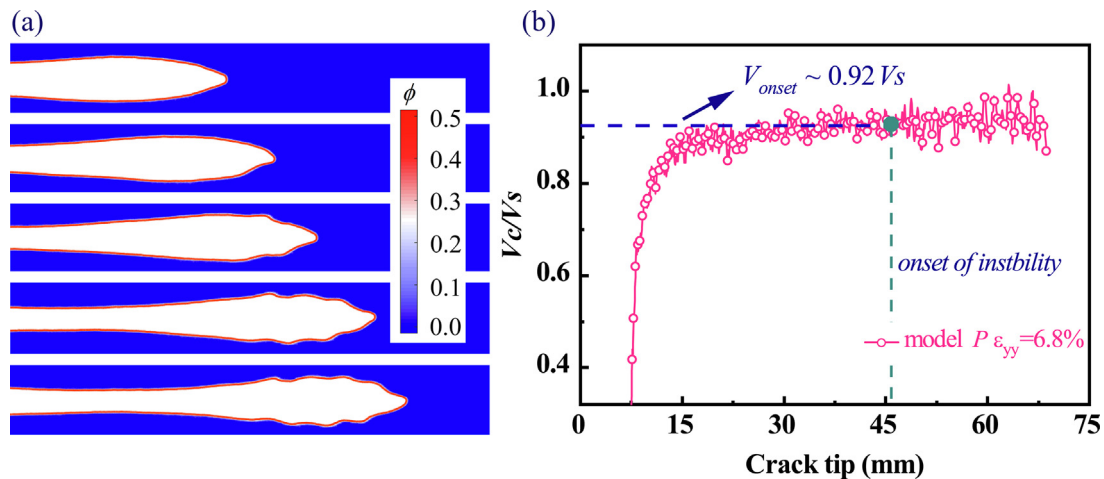
Fig. A1. (a) Oscillating crack patterns at a pre-strain of $\varepsilon_{yy} = 6.8\%$. (b) The corresponding normalized crack velocity profile V_C/V_S.

the non-physical attenuation of its wave velocity due to phase field damage. What we would like to emphasize in the end is that this study focuses on 2D fractures, in which the sprouting of micro-branches is suppressed. In the subsequent work, investigating the micro-branching instability with intrinsic 3D nature using the proposed model P would be a potential research interest.

Declaration of Competing Interest

The authors declare that they have no known competing financial interests or personal relationships that could have appeared to influence the work reported in this paper.

Acknowledgments

Appendix A

Supplementary data for crack oscillation instability

We recalculated the selfsame pre-strained fracture configuration using different material parameters from Section 5. The specific material parameters are set as $\mu = 36 \times 10^3$ Pa; $G_c = 2.4$ J/m^2; $\rho = 1290$ Kg/m^3; $l_0 = 1.5 \times 10^{-4}$ m The intrinsic shear wave velocity is calculated by $V_S = \sqrt{\mu/\rho} \sim 5.28$ m/s. At the background strain of $\varepsilon_{yy} = 6.8\%$, the captured crack oscillation patterns and the corresponding normalized crack velocity are presented in Fig. A1. Evidently, the crack velocity at the onset of oscillation instability is about $0.92V_S$, almost identical with Fig. 12. After the instability starts, the crack velocity also fluctuates significantly. Besides, we also tested several other sets of different material parameter inputs. Similar crack oscillations and ultra-high-speed crack tip splitting were observed without exception.

Appendix B. Supplementary data

Supplementary data to this article can be found online at https://doi.org/10.1016/j.ijsolstr.2020.07.004.

References

Ambati, M., Gerasimov, T., De Lorenzis, L., 2015. Phase-field modeling of ductile fracture. Comput. Mech. 55, 1017–1040.

Ambati, M., Kruse, R., De Lorenzis, L., 2016. A phase-field model for ductile fracture at finite strains and its experimental verification. Comput. Mech. 57, 149–167.

Aranson, I., Kalatsky, V., Vinokur, V., 2000. Continuum field description of crack propagation. Phys. Rev. Lett. 85, 118.

Bleyer, J., Molinari, J.-F., 2017. Microbranching instability in phase-field modelling of dynamic brittle fracture. Appl. Phys. Lett. 110, 151903.

Bleyer, J., Roux-Langlois, C., Molinari, J.-F., 2017. Dynamic crack propagation with a variational phase-field model: limiting speed, crack branching and velocity-toughening mechanisms. Int. J. Fract. 204, 79–100.

Borden, M.J., Hughes, T.J.R., Landis, C.M., Anvari, A., Lee, I.J., 2016. A phase-field formulation for fracture in ductile materials: Finite deformation balance law derivation, plastic degradation, and stress triaxiality effects. Comput. Methods Appl. Mech. Eng. 312, 130–166.

Borden, M.J., Verhoosel, C.V., Scott, M.A., Hughes, T.J.R., Landis, C.M., 2012. A phase-field description of dynamic brittle fracture. Comput. Methods Appl. Mech. Eng. 217–220, 77–95.

Bouchbinder, E., 2009a. Dynamic crack tip equation of motion: high-speed oscillatory instability. Phys. Rev. Lett. 103, 164301.

Bouchbinder, E., Fineberg, J., Marder, M., 2010a. Dynamics of simple cracks. Annu. Rev. Condens. Matter Phys. 1, 371–395.

Bouchbinder, E., Goldman, T., Fineberg, J., 2014. The dynamics of rapid fracture: instabilities, nonlinearities and length scales. Rep. Prog. Phys. 77, 046501.

Bouchbinder, E., Livne, A., Fineberg, J., 2008. Weakly nonlinear theory of dynamic fracture. Phys. Rev. Lett. 101, 264302.

Bouchbinder, E., Livne, A., Fineberg, J., 2010b. Weakly nonlinear fracture mechanics: experiments and theory. Int. J. Fract. 162, 3–20.

Bouchbinder, E., Mathiesen, J., Procaccia, I., 2005. Branching instabilities in rapid fracture: Dynamics and geometry. Phys. Rev. E 71, 056118.

Bouchbinder, E.J.P.r.l., 2009. Dynamic crack tip equation of motion: high-speed oscillatory instability. 103, 164301.

Bourdin, B., Francfort, G.A., Marigo, J.J., 2000. Numerical experiments in revisited brittle fracture. J. Mech. Phys. Solids 48, 797–826.

Bourdin, B., Francfort, G.A., Marigo, J.J., 2008. The Variational Approach to Fracture. J. Elast. 91, 5–148.

Bourdin, B., Larsen, C.J., Richardson, C.L., 2011. A time-discrete model for dynamic fracture based on crack regularization. Int. J. Fract. 168, 133–143.

Bourdin, B., Marigo, J.-J., Maurini, C., Sicsic, P., 2014. Morphogenesis and propagation of complex cracks induced by thermal shocks. Phys. Rev. Lett. 112, 014301.

Broberg, K.B., 1999. Cracks and fracture. Elsevier.

Buehler, M.J., Abraham, F.F., Gao, H., 2003. Hyperelasticity governs dynamic fracture at a critical length scale. Nature 426, 141–146.

Buehler, M.J., Gao, H., 2006. Dynamical fracture instabilities due to local hyperelasticity at crack tips. Nature 439, 307–310.

Chen, C.-H., Bouchbinder, E., Karma, A., 2017. Instability in dynamic fracture and the failure of the classical theory of cracks. Nat. Phys. 13, 1186–1190.

Fineberg, J., Bouchbinder, E., 2015. Recent developments in dynamic fracture: some perspectives. Int. J. Fract. 196, 33–57.

Fineberg, J., Gross, S., Sharon, E., 1997. Micro-branching as an instability in dynamic fracture, IUTAM Symposium on Nonlinear Analysis of Fracture. Springer, 177–189.

Fineberg, J., Gross, S.P., Marder, M., Swinney, H.L., 1991. Instability in dynamic fracture. Phys. Rev. Lett. 67, 457.

Fineberg, J., Marder, M., 1999. Instability in dynamic fracture. Phys. Rep. 313, 1–108.

Francfort, G.A., Marigo, J.J., 1998. Revisiting brittle fracture as an energy minimization problem. J. Mech. Phys. Solids 46, 1319–1342.

Freund, L.B., 1998. Dynamic fracture mechanics. Cambridge University Press.

Goldman, T., Harpaz, R., Bouchbinder, E., Fineberg, J., 2012. Intrinsic nonlinear scale governs oscillations in rapid fracture. Phys. Rev. Lett. 108, 104303.

Goldman, T., Livne, A., Fineberg, J., 2010. Acquisition of inertia by a moving crack. Phys. Rev. Lett. 104, 114301.

Hakim, V., Karma, A., 2009. Laws of crack motion and phase-field models of fracture. Journal of the Mechanics Physics of Solids 57, 342–368.

Heister, T., Wheeler, M.F., Wick, T., 2015. A primal-dual active set method and predictor-corrector mesh adaptivity for computing fracture propagation using a phase-field approach. Computer Methods in Applied Mechanics Engineering fracture mechanics 290, 466–495.

Henry, H., Levine, H., 2004. Dynamic instabilities of fracture under biaxial strain using a phase field model. Phys. Rev. Lett. 93, 105504.

Hesch, C., Weinberg, K., 2014. Thermodynamically consistent algorithms for a finite-deformation phase-field approach to fracture. Int. J. Numer. Meth. Eng. 99, 906–924.

Karma, A., Kessler, D.A., Levine, H., 2001. Phase-field model of mode III dynamic fracture. Phys. Rev. Lett. 87, 045501.

Karma, A., Lobkovsky, A.E., 2004. Unsteady Crack Motion and Branching in a Phase-Field Model of Brittle Fracture. Phys. Rev. Lett. 92, 245510.

Li, B., Bouklas, N., 2020. A variational phase-field model for brittle fracture in polydisperse elastomer networks. Int. J. Solids Struct. 182–183, 193–204.

Li, B., Maurini, C., 2019. Crack kinking in a variational phase-field model of brittle fracture with strongly anisotropic surface energy. Journal of the Mechanics Physics of Solids 125, 502–522.

Li, T., Marigo, J.J., Guilbaud, D., Potapov, S., 2016. Gradient damage modeling of brittle fracture in an explicit dynamics context. Int. J. Numer. Meth. Eng. 108, 1381–1405.

Livne, A., Ben-David, O., Fineberg, J., 2007. Oscillations in rapid fracture. Phys. Rev. Lett. 98, 124301.

Livne, A., Bouchbinder, E., Fineberg, J., 2008. Breakdown of linear elastic fracture mechanics near the tip of a rapid crack. Phys. Rev. Lett. 101, 264301.

Livne, A., Bouchbinder, E., Svetlizky, I., Fineberg, J., 2010. The near-tip fields of fast cracks. Science 327, 1359–1363.

Livne, A., Cohen, G., Fineberg, J., 2005. Universality and hysteretic dynamics in rapid fracture. Phys. Rev. Lett. 94, 224301.

Loew, P.J., Peters, B., Beex, L.A., 2019. Rate-dependent phase-field damage modeling of rubber and its experimental parameter identification. Journal of the Mechanics Physics of Solids 127, 266–294.

Lubomirsky, Y., Chen, C.-H., Karma, A., Bouchbinder, E., 2018. Universality and stability phase diagram of two-dimensional brittle fracture. Phys. Rev. Lett. 121, 134301.

Mao, Y., Anand, L., 2018. A theory for fracture of polymeric gels. Journal of the Mechanics Physics of Solids 115, 30–53.

Mesgarnejad, A., Imanian, A., Karma, A., 2019. Phase-field models for fatigue crack growth. Theor. Appl. Fract. Mech. 103, 102282.

Miehe, C., Hofacker, M., Welschinger, F., 2010a. A phase field model for rate-independent crack propagation: Robust algorithmic implementation based on operator splits. Comput. Methods Appl. Mech. Eng. 199, 2765–2778.

Miehe, C., Schänzel, L.-M., 2014. Phase field modeling of fracture in rubbery polymers. Part I: Finite elasticity coupled with brittle failure. Journal of the Mechanics Physics of Solids 65, 93–113.

Miehe, C., Welschinger, F., Hofacker, M., 2010b. Thermodynamically consistent phase-field models of fracture: Variational principles and multi-field FE implementations. Int. J. Numer. Meth. Eng. 83, 1273–1311.

Moutsanidis, G., Kamensky, D., Chen, J.S., Bazilevs, Y., 2018. Hyperbolic phase field modeling of brittle fracture: Part II—immersed IGA–RKPM coupling for air-blast–structure interaction. J. Mech. Phys. Solids 121, 114–132.

Murphy, N., Ali, M., Ivankovic, A., 2006. Dynamic crack bifurcation in PMMA. Eng. Fract. Mech. 73, 2569–2587.

Patil, R., Mishra, B., Singh, I., Bui, T., 2018. A new multiscale phase field method to simulate failure in composites. Adv. Eng. Softw. 126, 9–33.

Ravi-Chandar, K., 2004. Dynamic fracture. Elsevier.

Ravi-Chandar, K., Knauss, W., 1984. An experimental investigation into dynamic fracture: III. On steady-state crack propagation and crack branching. Int. J. Fract. 26, 141–154.

Sharon, E., Gross, S.P., Fineberg, J., 1995. Local Crack Branching as a Mechanism for Instability in Dynamic Fracture. Phys. Rev. Lett. 74, 5096–5099.

Sharon, E., Gross, S.P., Fineberg, J., 1996. Energy dissipation in dynamic fracture. Phys. Rev. Lett. 76, 2117.

Shen, R., Waisman, H., Guo, L., 2019. Fracture of viscoelastic solids modeled with a modified phase field method. Computer Methods in Applied Mechanics Engineering fracture mechanics 346, 862–890.

Swope, W.C., Andersen, H.C., Berens, P.H., Wilson, K.R., 1982. A computer simulation method for the calculation of equilibrium constants for the formation of physical clusters of molecules: Application to small water clusters. J. Chem. Phys. 76, 637–649.

Tang, S., Zhang, G., Guo, T.F., Guo, X., Liu, W.K., 2019. Phase field modeling of fracture in nonlinearly elastic solids via energy decomposition. Computer Methods in Applied Mechanics Engineering fracture mechanics 347, 477–494.

Tanné, E., Li, T., Bourdin, B., Marigo, J.-J., Maurini, C., 2018. Crack nucleation in variational phase-field models of brittle fracture. J. Mech. Phys. Solids 110, 80–99.

Tian, F., Tang, X., Xu, T., Li, L., 2019a. An adaptive edge-based smoothed finite element method (ES-FEM) for phase-field modeling of fractures at large deformations. arXiv preprint arXiv:.10858.

Tian, F., Tang, X., Xu, T., Yang, J., Li, L., 2019b. A hybrid adaptive finite element phase-field method for quasi-static and dynamic brittle fracture. Int. J. Numer. Meth. Eng. 120, 1108–1125.

Wu, J.-Y., Nguyen, V.P., 2018. A length scale insensitive phase-field damage model for brittle fracture. J. Mech. Phys. Solids 119, 20–42.

Wu, J.-Y., Nguyen, V.P., Nguyen, C.T., Sutula, D., Bordas, S., Sinaie, S., 2018. Phase field modeling of fracture. Advances in Applied Mechancis: Multi-scale Theory. Comput. Mech. 52.

Wu, J., McAuliffe, C., Waisman, H., Deodatis, G., 2016. Stochastic analysis of polymer composites rupture at large deformations modeled by a phase field method. Computer Methods in Applied Mechanics Engineering 312, 596–634.

Yin, B., Kaliske, M., 2020. Fracture simulation of viscoelastic polymers by the phase-field method. Comput. Mech. 65, 293–309.

Zhang, P., Hu, X., Bui, T.Q., Yao, W., 2019. Phase field modeling of fracture in fiber reinforced composite laminate. Int. J. Mech. Sci. 161, 105008.